PCCP

ROYAL SOCIETY OF CHEMISTRY

PAPER

View Article Online
View Journal | View Issue

Cite this: *Phys. Chem. Chem. Phys.*, 2022, **24**, 13376

FeP_2 monolayer: isoelectronic analogue of MoS_2 with excellent electronic and optical properties†

Chen Yan,[a] Jiuqi Yi,[a] Dan Li,*[a] Chang Xu[a] and Longjiu Cheng *[ab]

Received 4th March 2022,
Accepted 10th May 2022

DOI: 10.1039/d2cp01057g

rsc.li/pccp

Two-dimensional semiconductors with suitable indirect band gaps, excellent light absorption capacity, and oxidation resistance are particularly suitable for material applications. Here based on first-principle calculations, we report that the FeP_2 monolayer, which is isoelectronic with MoS_2, has novel electronic properties and an ultra-low diffusion energy barrier of K on the surface, indicating its potential as an anode material of K-ion batteries. The calculated phonon dispersion curves, molecular dynamics, and elastic constants showed that it has high structural stability and oxidation resistance. The monolayer was a semiconductor with an indirect band gap of 0.68 eV. In addition, the FeP_2 monolayer had obvious light absorption in the infrared, visible, and ultraviolet regions, which can be widely used in optoelectronic devices. Bonding analysis showed that there were multicenter bonds inside every hexagonal ring. As the anode material of K-ion batteries, the FeP_2 monolayer had a capacity of 456.84 mA h g^{-1}, low diffusion energy barrier, and open-circuit voltage. All these characteristics suggest that the FeP_2 monolayer is a potential anode material for K-ion batteries, which needs to be further verified by experiments.

Introduction

Since the discovery of graphene with a unique structure and physical properties in 2004,[1] an increasing number of researchers have been attracted to study two-dimensional (2D) materials.[2–7] The calculation and prediction of new 2D materials can provide researchers with insights for synthesizing new materials, such as Cu_2Si,[8] Ti_3C_2,[9] and germanene,[10] These materials were predicted by theoretical calculations and then synthesized through experiments. In the past decade, transition metal dichalcogenides (TMDCs) have been considered as promising 2D materials for functional devices because of their special electronic, optical, and tribological properties,[11–14] such as MoS_2,[15] $MoSe_2$,[16] WS_2,[17] and NiS_2.[18] The most typical one is the MoS_2 monolayer, which has a direct band gap of 1.8 eV,[19] and has excellent mechanical properties and a high charge mobility,[20] supporting its broad use in flexible electronic devices and as a solid lubricant in spacecraft.[21–25] Moreover, the MoS_2 monolayer has been widely studied in the fields of photoelectron and photocatalysis due to its special crystal structure, energy band structure, high chemical stability, and catalysis.[26–30] Besides, two-dimensional (2D) MoS_2 has been studied theoretically and experimentally as an anode material for lithium-ion batteries (LIBs),[31,32] sodium-ion batteries (NIBs), and potassium-ion batteries (KIBs).[33–37] In recent years, Fe–P monolayers have attracted much attention on account of their high natural richness, low cost, good electrical conductivity, and structural stability. Zhang *et al.* predicted that the FeP_3 monolayer would exhibit excellent catalytic activity in the hydrogen evolution reaction (HER) of electrolytic water.[38] The Fe_3P monolayer with anisotropic high-temperature ferromagnetism is a promising candidate for spintronic nanodevices.[39]

In the past two decades, LIBs have been widely used in electronic devices and electric vehicles due to their long cycle life and high energy density.[40–42] However, the scarcity of Li and long charging time limit its wide-scale applications.[43] Therefore, we need to find cheaper and more powerful alternatives. In recent years, NIBs and KIBs have attracted more and more attention because of their rich abundance on the earth and similar chemical properties to Li.[44–46] However, compared with NIBs, KIBs have a higher energy density and operating voltage, so it is very important to find good anode materials for KIBs.

Taking the low cost of Fe–P monolayers and the characteristics of 2D MoS_2 into account, we predict an FeP_2 monolayer, which is isoelectronic with the MoS_2 monolayer. Compared with MoS_2 monolayers, FeP_2 monolayers are cheaper, safer, and more environmentally friendly. In addition, FeP_2 and MoS_2 monolayers have some similar properties in the air, such as good oxidation resistance. FeP_2 monolayers have better optical

[a] *Department of Chemistry, Key Laboratory of Functional Inorganic Materials of Anhui Province, Anhui University, Hefei, Anhui 230601, P. R. China. E-mail: clj@ustc.edu, ahulidan@aliyun.com*
[b] *Key Laboratory of Structure and Functional Regulation of Hybrid Materials (Anhui University), Ministry of Education, Hefei, 230601, P. R. China*

† Electronic supplementary information (ESI) available. See DOI: https://doi.org/10.1039/d2cp01057g

properties and are more suitable as anode materials for KIBs, so they can be used to replace MoS_2 monolayers in optical and KIBs applications. In this work, the structural character, chemical stability, and mechanical and electronic properties of FeP_2 monolayers were calculated by density functional theory (DFT). The optical properties of FeP_2 monolayers were calculated and compared with MoS_2 monolayers. Besides, our computations demonstrated that the FeP_2 monolayer possessed low diffusion barriers and a high capacity as an anode material for KIBs. The discovery of these special properties can make FeP_2 monolayers have great application prospects as photoelectric materials and anode materials for KIBs.

Computational method

DFT calculations were carried out in the Vienna *Ab initio* Simulations Package (VASP),[47–50] with the projector-augmented wave (PAW) method used to deal with the interaction between electrons and ions.[51] The exchange–correlation functional was treated through the generalized gradient approximation (GGA)[52] in the form of Perdew–Burke–Ernzerhof (PBE).[53] The energy and the force standard received on each atom were set to 10^{-6} eV and 0.01 eV $Å^{-1}$, respectively. The energy cutoff of the plane wave was set to 400 eV, and a $13 \times 13 \times 1$ Monkhorst–Pack[54] *k*-grid for Brillouin zone sampling was used for the geometry optimization and self-consistent calculations. To avoid the influence between adjacent layers, the FeP_2 monolayer was placed on the *xy* plane with the *z* direction perpendicular to the layer plane, and a vacuum space of 30 Å was used in the *z* direction.

The calculation of the phonon spectra was completed in the PHONOPY program.[55] Also, the phonon spectrum of a $2 \times 2 \times 1$ supercell was calculated. In the *ab initio* molecular dynamics (AIMD) simulation, the *NVT* canonical ensemble was adopted, and $6 \times 6 \times 1$ supercells were considered. The simulation lasted for 5.0 ps with a time step of 1.0 fs, and the temperature was controlled by using the Nosé–Hoover method.[56] Because PBE tended to underestimate the energy band gap, we used the HSE06[57] hybrid function to calculate a more accurate electronic band structure and optical properties.

Chemical bonding analysis of the FeP_2 monolayer was performed using the solid-state adaptive natural density partitioning (SSAdNDP) method,[58] which was developed by Boldyrev *et al.*[59–62] We chose the def2-TZVP[63] basis set as the plane-wave projection of the electron density matrix. The climbing-image nudged elastic band (CI-NEB) method[64] was employed to study the adsorption kinetics of O_2 molecules. To this end, a $4 \times 4 \times 1$ supercell was established, which contained 16 Fe atoms and 32 P atoms. Nine images were used to calculate the reaction path. The long-range van der Waals (vdW) interaction between O_2 molecule and FeP_2 monolayer was considered by the DFT-D3 method.[65] Similarly, when the FeP_2 monolayer was assessed as the anode material for KIBs, the CI-NEB method was used to explore the lowest energy barriers and diffusion path of K atoms on the FeP_2 monolayer, and the vdW interactions were considered by the semiempirical DFT-D2 method.[66] This method has been proved to be a reliable K content adsorption method for the efficient identification of graphene-based materials.[33] Each intermediate image of the CI-NEB simulation was relaxed until the perpendicular force was less than 0.02 eV $Å^{-1}$. All the crystal structures were visualized using the VESTA software package.[67]

Results and discussion

Fig. 1(a) shows the monolayer structure of FeP_2, in which one unit cell of an FeP_2 monolayer consists of one Fe atom and two P atoms. Like the structure of MoS_2, a Fe atom is sandwiched between two P atoms. The optimized lattice parameters of the FeP_2 monolayer were found to be $a = b = 2.78$ Å, the thickness was 3.27 Å, and the Fe–P bond length was 2.29 Å. To evaluate the energetic stability of the FeP_2 monolayer, we calculated the formation energy ΔH, defined as

$$\Delta H = \frac{E_{\text{total}} - n_1 \times E_{\text{Fe}} - n_2 \times E_{\text{P}}}{n} \quad (1)$$

where E_{total} is the total energy of FeP_2, and E_{Fe} and E_{P} are the energies per atom of the face-centered cubic (fcc) Fe and triclinic P_{24} solids, respectively. The factors n_1 and n_2 are the atomic numbers of Fe and P, while the factor n is the total atomic number in the unit cell. The calculated ΔH was negative (−0.11 eV per atom), indicating that the formation of the substance was exothermic and could exist stably. We calculated the phonon spectrum to assess its dynamic stability. As shown in Fig. 1(b), the fact that it had no imaginary phonon mode in the whole Brillouin zone confirmed that our predicted FeP_2 was dynamically stable. To evaluate its thermal stability, we performed AIMD simulation at 300, 400, and 500 K. It can be seen in Fig. 1(c) that the framework of the FeP_2 monolayer remained intact without disruption at the temperature of 300 K, which showed its thermal stability. We further simulated AIMD at 400 and 500 K, as shown in Fig. S5 (ESI†), indicating that the FeP_2 monolayer could also be stable at 400 K. However, at the temperature of 500 K, the structure was disrupted, which showed that its melting point was between 400 and 500 K.

By calculating the elastic constants of its materials, its mechanical properties were studied. The calculated elastic constants, Young's modulus, and Poisson's ratio are shown in Table 1.

For mechanically stable 2D materials, the elastic constants need to satisfy $C_{11}C_{22} - C_{12}^2$ and $C_{66} > 0$.[68,69] Obviously, the calculated elastic constants satisfied this condition, indicating its mechanical stability. Young's modulus is a physical quantity that describes the ability of a material to resist deformation, and it reflects the flexibility or rigidity of materials. The Young's modulus of a flexible material is lower. It can be seen that the Young's modulus of 2D FeP_2 was 69.53 N m^{-1}, which is lower than most the 2D materials reported so far, such as graphene (344 N m^{-1}),[70] MoS_2 (123 N m^{-1}),[71] and 2D phosphoborane (142.5 N m^{-1}),[62] but in the same order of magnitude as silicene (65 N m^{-1}).[72] This shows that the FeP_2 monolayer deforms

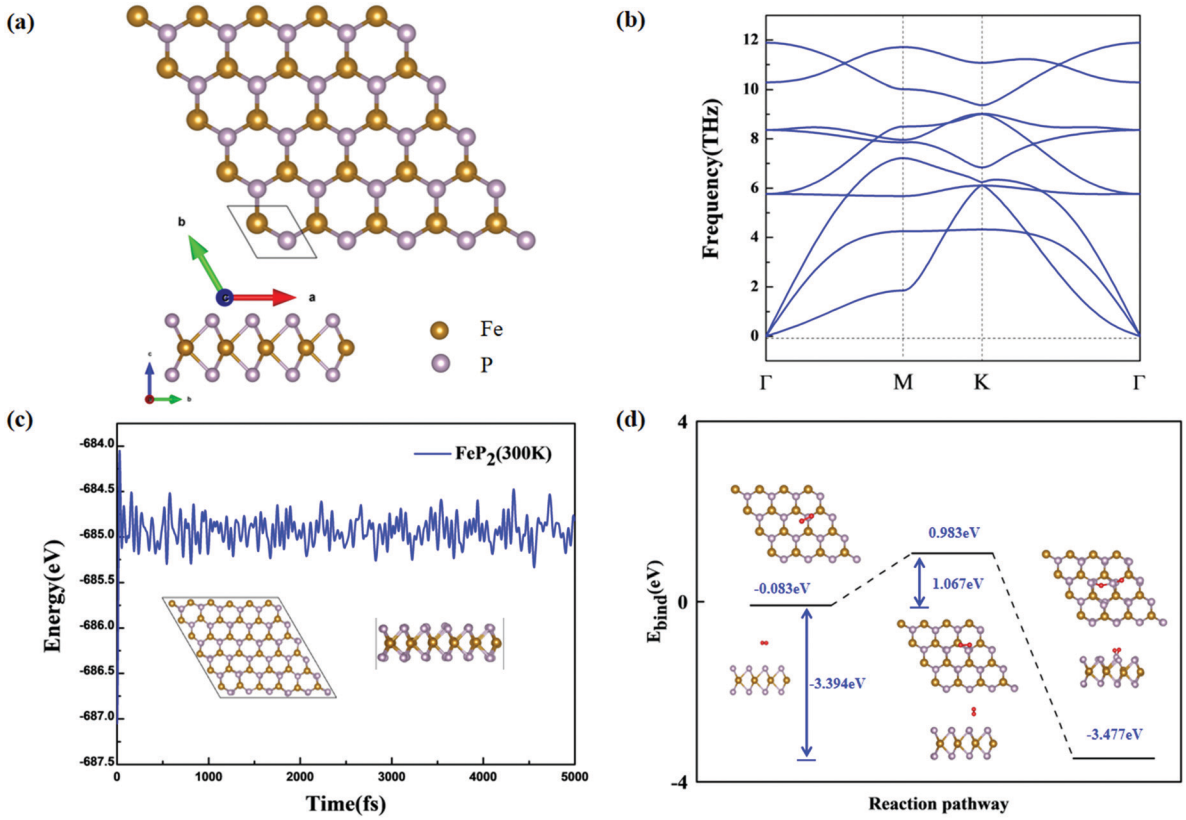

Fig. 1 (a) Top and side views of the optimized geometric structures of the FeP_2 monolayer. (b) Phonon spectra of the FeP_2 monolayer. (c) AIMD simulation of the FeP_2 monolayer at 300 K, with a variation of the energy fluctuation with time step, and a snapshot of the FeP_2 monolayer. (d) The reaction pathway and energy barrier from physisorption to chemisorption of an O_2 molecule on the FeP_2 monolayer.

Table 1 Calculated elastic constants (C_{ij}, N m^{-1}), Young's modulus (E_{2D}, N m^{-1}), and Poisson's ratio (ν) of the FeP_2 monolayer

Structure	C_{11}/C_{22}	C_{12}	C_{66}	E_{2D}	ν
FeP_2	78.25	26.12	26.07	69.53	0.33

greatly under external stresses. Therefore, the FeP_2 monolayer has a strong sensitivity to its elastic deformation and has favorable mechanical flexibility. Like MoS_2 monolayers, the FeP_2 monolayer is a soft material that is expected to be used in flexible batteries and electronic devices. The Poisson's ratio of the FeP_2 monolayer was calculated to be 0.33, which is within the reasonable range of 2D materials (0–0.5). The spin-polarized calculation confirmed that the FeP_2 monolayer was in a diamagnetic ground state, indicating that there were no unpaired electrons or dangling bonds.

As is well known, phosphorene has excellent properties, but it is easy to be oxidized in air, which greatly restricts its applications.[73] Therefore, it is vital to consider the oxidation resistance of the FeP_2 monolayer. The energy barrier from physisorption to chemisorption of an O_2 molecule on the FeP_2 monolayer surface was investigated by the CI-NEB method. The binding energy of the monolayer and O_2 interaction is defined as

$$E_{bind} = E_{total} - E_{FeP_2} - E_{O_2} \quad (2)$$

where E_{total}, E_{FeP_2}, and E_{O_2} are the energies of the FeP_2 monolayer adsorbed by an O_2 molecule, the FeP_2 monolayer, and a single O_2 molecule in the triplet spin state, respectively. By definition, the more negative the E_{bind}, the stronger the adsorption. Fig. S1 (ESI†) shows the physical adsorption of O_2 molecules at several different positions on the FeP_2 monolayer. We choose the structure with the lowest E_{bind} (−0.083 eV) to simulate the oxidation process.

As shown in Fig. 1(d), in the stage of physisorption, the O_2 molecule was located 3.6 Å above the surface of the FeP_2 monolayer, the O–O bond length was 1.23 Å, and the binding energy was −0.083 eV. In the transition state, the O_2 molecule was located 2.24 Å above the surface of the FeP_2 monolayer, and the O–O bond length was elongated to 1.27 Å. The transition from physisorption to chemisorption required the O_2 molecule to overcome an activation energy of 1.067 eV. The calculated activation energy was much higher than that of phosphorene (0.700 eV).[74] It is equivalent to PC_6 (1.080 eV)[75] under air stability, indicating that FeP_2 might be chemically stable in air. To further confirm this result, we carried out AIMD simulations of FeP_2 and O_2 molecules at 300 K, using a 6 × 6 × 1 supercell. As shown in Fig. S2 (ESI†), the O_2 molecules move away from the FeP_2 monolayer, rather than dissociate

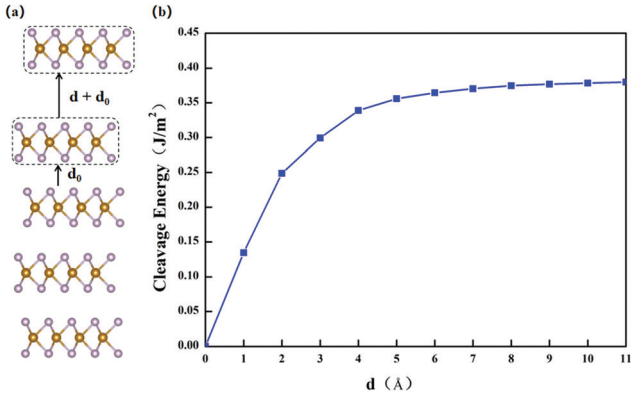

Fig. 2 (a) Separating a monolayer from its neighboring four layers. (b) Cleavage energy as a function of the separation distance for a fracture in the FeP_2 bulk.

into oxygen atoms after 5 ps. As a result, the FeP_2 monolayer exhibited good chemical inertness in air.

To obtain the possibility of FeP_2 monolayers, a mechanical exfoliation strategy was used. The cleavage energy E_{cl} for separating a FeP_2 monolayer from a neighboring four layers was calculated. E_{cl} is defined as the minimum energy required during the exfoliation process. We first established a five-layer slab, in which four layers were fixed and the top monolayer was flexible, as shown in Fig. 2. The cleavage energy was calculated by increasing the separation distance d. Finally, the distance d_0 between layers was calculated to be 3.50 Å. With the increase in d, the cleavage energy gradually converged to a constant value of $\sim$0.38 J m^{-2}. Notably, the calculated cleavage energy was equivalent to that of graphene (0.37 J m^{-2})[76] and MoS_2 (0.30 J m^{-2}),[77] indicating a high possibility of separating FeP_2 monolayers in experiments.

The band structure and projected density of states (PDOS) of the FeP_2 monolayer were computed using the HSE06 functional, as shown in Fig. 3. The valence band maximum (VBM) of the structure was located at the M point, and the conduction band minimum (CBM) was located at the K point, which indicates that the FeP_2 monolayer was an indirect semiconductor with a band gap of 0.68 eV. Through PDOS analysis, VBM and CBM were found to be mainly contributed to by the Fe-d orbital and the P-p orbital.

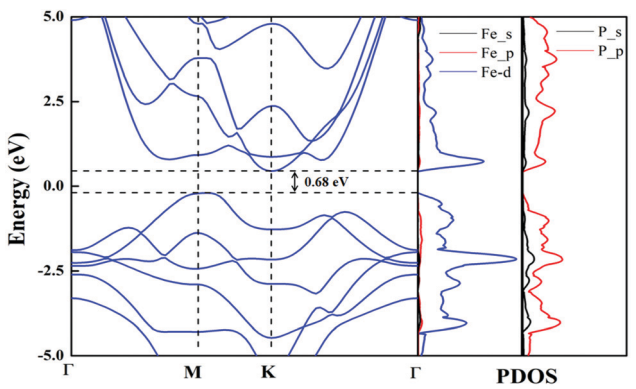

Fig. 3 Electronic band structure and PDOS of the FeP_2 monolayer at the HSE06 level.

The interpretation of the FeP_2 monolayer bonding picture is an important step in understanding the nature of this unique and multifunctional material. To deeply understand the bonding nature and stabilizing mechanism of the FeP_2 monolayer, we calculated the electron localization function (ELF). Generally, the values 1.00 and 0.50 correspond to a fully localized localization of electrons and fully delocalized electrons, respectively, while a value near 0.00 implies an area with low electron density. To highlight the multicenter bonds in the hexagonal rings, we drew ELF maps at the different highest points. As shown in Fig. 4, there was a triangle-like area of electron localization probability inside the rings, indicating the existence of multicenter bonds in the rings.

We used the SSAdNDP method to further examine the chemical bonding pattern of the FeP_2 monolayer ($4 \times 4 \times 1$ supercell), as visualized in Fig. 5. This showed that every phosphorus had one lone pair (1c–2e) with occupation numbers (ONs) of 1.81 $|e|$. Every Fe atom was bonded to six neighboring P atoms by two-center-two-electron (2c–2e) bonds with ONs = 1.85 $|e|$. After localization of all the lone pairs on P and 2c–2e bonds, 32 out of 288 valence electrons remained unlocalized in our supercell. We tested 1c–2e bonds on Fe atoms, but found that the occupation numbers were about 0.5–0.6 $|e|$. Therefore, there may be multicenter bonds present. After that, the bonding of three Fe atoms in hexagonal rings was tested, and 3c–2e multicenter bonds were found. The occupation number was 1.45 $|e|$. As this numerical value was not very large, we continued to look for multicenter bonds of more atoms. Hence, we found that three Fe and six P atoms formed 9c–2e bonds with ONs = 1.93 $|e|$, and the occupation numbers of 1.93 $|e|$ mainly came from Fe atoms. Therefore, the abundance of multicenter bonds led to robust connections between the Fe and P atoms, thus, enhancing the stability of the structure.

Recent studies have shown that 2D materials with narrow band gaps can serve as good infrared photodetectors and solar energy harvesters.[78,79] Thus, the absorption coefficient was calculated by the HSE06 functional to further explore the optical properties of the FeP_2 monolayer. The FeP_2 monolayer has no anisotropy in the x- and y-directions, so we only

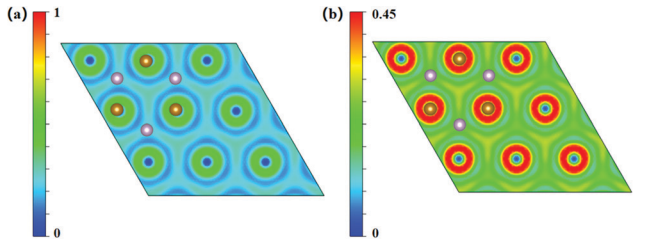

Fig. 4 ELF slice with 001 Miller indices. (a) The color of red and blue refer to the highest (1.00) and the lowest value (0.00) of ELF. (b) The color of red and blue refer to the highest (0.45) and the lowest value (0.00) of ELF. The isosurface value is 0.54. Brown and white balls represent Fe and P atoms, respectively.

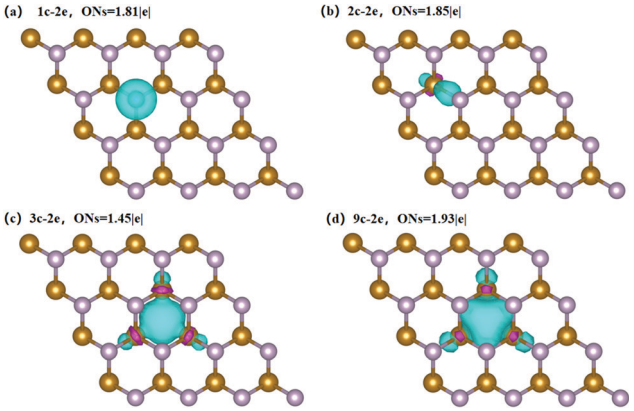

Fig. 5 Schematic of SSAdNDP chemical bonding patterns for the FeP_2 monolayer. The isosurface value was 0.06.

analyzed the optical properties in the *x*-direction, which is similar to 2D MoS_2. As shown in Fig. 6(a), the area within the dotted line is the visible light range. It can be seen that the FeP_2 monolayer not only exhibited good optical absorption in the visible and ultraviolet regions, but also had large absorption in the infrared region. In contrast, the MoS_2 monolayer only had significant light absorption in the ultraviolet and visible regions. It is well known that 43% of the solar energy is in the infrared region and that the MoS_2 monolayer is an excellent sunlight absorber. Therefore, the FeP_2 monolayer may be a better solar absorber than the MoS_2 monolayer and can also be used as an infrared photodetector. These results indicate that the FeP_2 monolayer will be a very promising material for future optoelectronic devices.

The FeP_2 monolayer is a narrow band gap semiconductor that can form a metallic state when absorbing metal ions, thus promoting electrical conductivity. Consequently, we then investigated the adsorption and diffusion behavior of the isolated K atom on the surface of the FeP_2 monolayer. A $4 \times 4 \times 1$ supercell was adopted to find the most stable adsorption site for K. According to the symmetry of the FeP_2 monolayer, we considered five possible adsorption sites, which are shown in Fig. 6(b). The adsorption energy (E_{ad}) is evaluated using

$$E_{ad} = E_{K+FeP_2} - E_{FeP_2} - E_K \quad (3)$$

where E_{K+FeP_2}, E_{FeP_2} and E_K are the total energies of K-adsorbed, pure FeP_2 monolayers and the energy per atom in bulk K, respectively. By definition, more negative adsorption energy indicates more stable adsorption of K on the FeP_2 monolayer.

The A_1 and A_2 adsorption sites are located directly above the Fe and S atoms, respectively. The A_3 is located in the center of the hexagon composed of Fe and P atoms, the A_4 site represents the center of two adjacent Fe atoms, and the A_5 site denotes the center of Fe and P atoms. After structural relaxation, there were only three inequivalent stable adsorption sites. The adsorption sites of A_4 and A_5 were unstable and the K atom transformed to the A_1 site. The adsorption energy is shown in Table S1 (ESI†). Among the three stable adsorption sites, the A_1 site was the most favorable with an adsorption energy of −1.78 eV.

We calculated the charge density difference to examine the adsorption interaction of the K atom and FeP_2 monolayer, as indicated in Fig. 6(c). The yellow and blue regions represent the accumulation and the decreasing trend of charge, respectively.

It can be clearly seen that the charge accumulated on the FeP_2 monolayer and the charge depletion occurred around the K atom, indicating that electrons were transferred from the K atom to the FeP_2 monolayer during the adsorption of the K atom. Further Bader charge analysis showed that 0.76 $|e|$ was transferred from the K atom to the FeP_2 monolayer. Additionally, the band structure of K atom intercalated FeP_2 monolayer is illustrated in Fig. S3 (ESI†). We found that the FeP_2 monolayer turned into a metallic state after adsorption of the K atom, ensuring good electrical conductivity during the battery cycle.

On the other hand, the diffusion energy barrier of K on the FeP_2 surface is closely related to the charge/discharge rate of the battery. Hence, the CI-NEB method was used to estimate the diffusion barriers. Considering the stable adsorption sites of A_1, A_2, and A_3, and the K atoms preferring to occupy the A_1

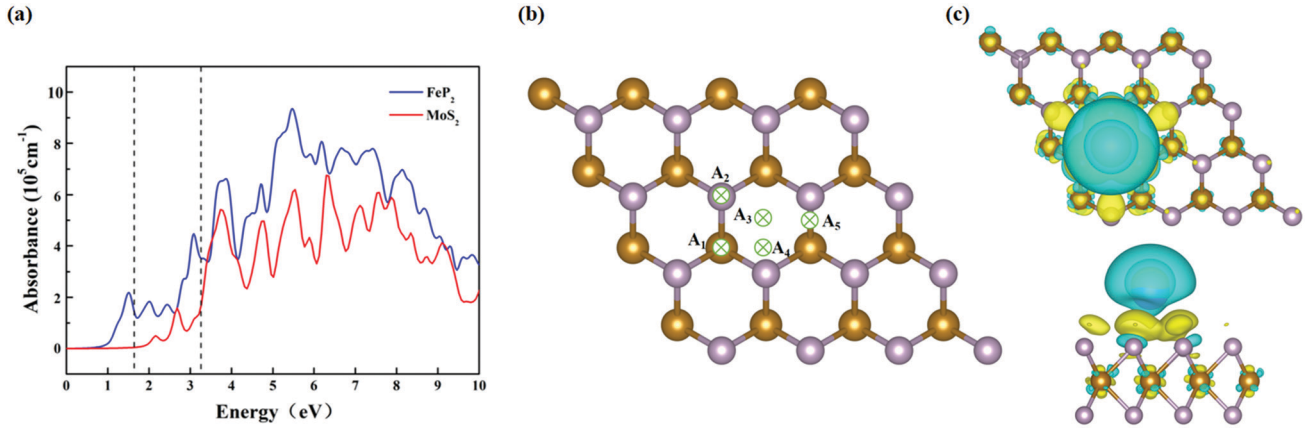

Fig. 6 (a) Light absorption spectra of FeP_2 and MoS_2 monolayers calculated by the HSE06 method. (b) Different adsorption sites of K ions on the surface of the FeP_2 monolayer. (c) Charge density difference of K ions on the FeP_2 monolayer.

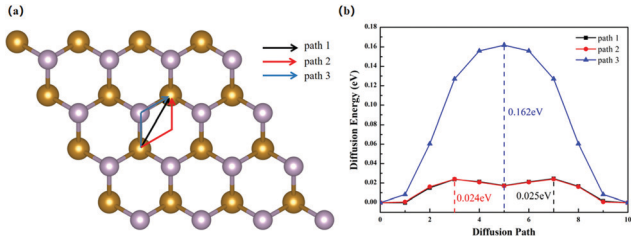

Fig. 7 (a) The migration paths of K diffusion on the FeP_2 monolayer. (b) The diffusion barrier profiles for K migration for the considered three paths.

site, there were three possible diffusion pathways, as shown in Fig. 7(a). For path I, the K ion migrates directly from the A_1 site to the adjacent A_1 site, and the resulting diffusion energy barrier is 0.025 eV. For path II, the K ion moves from the A_1 site to the A_3 site, and then to another the A_1 site, with a diffusion energy barrier of 0.024 eV. For path III, the K ion moves from the A_1 site to the A_2 site, and then to another A_1 site, with a diffusion energy barrier of 0.162 eV, as shown in Fig. 7(b). The diffusion energy barrier of path II was the lowest, only 0.024 eV. It was also significantly lower than the commercial graphite anode from LIBs (0.400 eV)[80,81] and even lower than the diffusion energy barrier of MoS_2 (0.063 eV)[33] as an anode material.

The storage capacity of K atoms is an important property of the battery, which is directly proportional to the number of adsorbed K atoms on the surface. Therefore, to explore the capacity, different contents of K (x = 0.125, 0.500, 1.000, 1.500) were added to both sides of the FeP_2 monolayer, and the average adsorption energy was calculated to examine the adsorption stability, which is defined as

$$E_{ave} = \frac{E_{K+FeP_2} - E_{FeP_2} - nE_K}{n} \quad (4)$$

where n is the number of adsorbed K atoms, E_{K+FeP_2} and E_{FeP_2} are the total energies of the K-adsorbed and pure FeP_2 monolayers, respectively. Similarly, as long as E_{ave} is negative, the K atoms can be adsorbed stably.

Since the adsorption energy of the A_1 site was the largest, and adsorption on both sides can reduce the Coulomb repulsion between K ions, the adsorption sites on both sides of A_1 were first adopted. As clearly shown in Fig. 8, when the K content was 0.125 and 0.500, E_{ave} was −1.730 and −1.070 eV, respectively. The distance between K ions was too close, which led to Coulombic repulsion when the K content was at x = 1.000. The K ions were displaced from the A_1 sites on both sides of the FeP_2 monolayer, so we considered A_2 sites with slightly weaker adsorption energy, and E_{ave} was −0.835 eV. At the same time, we considered the adsorption of K at the A_1 site on the same side. Although there was no displacement, the calculated average adsorption energy was 0.076 eV, which is obviously unstable. At x = 1.500, we also considered that all K ions were adsorbed on both sides of the A_1 and A_2 sites, and the K ions were displaced. To reduce the Coulombic repulsion between K ions, they were adsorbed on both sides of A_1, A_2, and A_3 sites, and E_{ave} was −0.56 eV. To sum up, the adsorption of K contents at x = 0.125, 0.500, 1.000, and 1.500 on the FeP_2 monolayer is favorable and the structure energy is stable. At x = 2.000, due to the large number and radius of K ions, they could not be adsorbed stably on the A_1, A_2, and A_3 sites of the FeP_2 monolayer at the same time. Accordingly, the maximum content of K that could be adsorbed on the FeP_2 monolayer was 1.500.

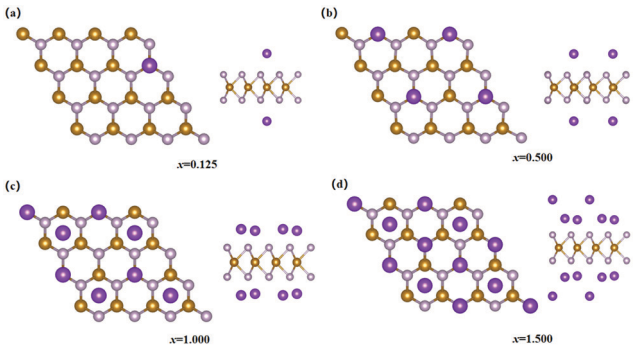

Fig. 8 Structures of the K adsorption models on different concentrations of FeP_2, including x = (a) 0.125, (b) 0.500, (c) 1.000, and (d) 1.500.

We calculated the storage capacity of K ions by the formula $C = xF/M$. In this formulation, M, F, and x define the molecular mass of FeP_2, the Faraday constant (28601 mA h mol^{-1}), and the concentration of the adsorbed K ions (x = 1.500 in this work) per unit FeP_2. The calculated maximum storage capacity of the FeP_2 monolayer was 456.84 mA h g^{-1}, which was larger than those of graphite (273 mA h g^{-1})[46] and MoS_2 monolayers (334.86 mA h g^{-1})[33] as an anode material for KIBs. Finally, we investigated the open-circuit voltage (OCV) of the FeP_2 monolayer. The OCV during charging/discharging can be obtained by the following reaction: $FeP_2 + xK^+ + xe^- \leftrightarrow FeP_2Kx$. Thus, ignoring the contribution of volume and entropy,[82] the average OCV can be evaluated by[83]

$$OCV = \frac{E_{FeP_2} + mE_K - E_{mK+FeP_2}}{me} \quad (5)$$

where m is the concentration of the adsorbed K atoms. It was clearly found that as the K concentration increased, the OCV dropped from 1.725, 1.069, 0.835, to 0.557 V, as shown in Fig. S4 (ESI†). This shows that there was a steady voltage change during cycling. The OCV at the final stage was as low as 0.557 V, which is within the working voltage range (01.0 V) of anode materials.[84,85] Based on these results, FeP_2 monolayers are a promising candidate anode material for KIBs.

Conclusions

In summary, we successfully predicted an FeP_2 monolayer that is isoelectronic with MoS_2. By means of DFT investigation, the FeP_2 monolayer demonstrated good dynamic, mechanical, and thermal stabilities. The low cleavage energy indicates that it is feasible to exfoliate monolayers from the bulk structure. We also verified that the FeP_2 monolayer can resist oxidation in air. The electron properties calculated by the HSE06 method

showed that the FeP_2 monolayer is a semiconductor with an indirect band gap of 0.68 eV, and has light absorption in the infrared, visible, and ultraviolet regions. Chemical bonding analysis showed that there are 9c–2e bonds in every hexagonal ring of the FeP_2 monolayer. The storage capacity of the FeP_2 monolayer as an anode material of KIBs reached 456.84 mA h g^{-1}. Moreover, the diffusion barrier was as low as 0.024 eV and had a low OCV. All the calculation results show that the FeP_2 monolayer has potential application prospects in electronic and optoelectronic devices, and as an anode material for KIBs. Moreover, because of its low cost, high safety, and excellent optical properties, the FeP_2 monolayer is expected to replace the MoS_2 monolayer in the fields of solar absorption devices and anode materials for KIBs.

Conflicts of interest

There are no conflicts of interest to declare.

Acknowledgements

This work is financed by the National Natural Science Foundation of China (21873001), and by the Foundation of Distinguished Young Scientists of Anhui Province. The calculations are carried out at the High-Performance Computing Center of Anhui University.

Notes and references

1 K. S. Novoselov, A. K. Geim, S. V. Morozov, D. Jiang, Y. Zhang, S. V. Dubonos, I. V. Grigorieva and A. A. Firsov, *Science*, 2004, **306**, 666–669.
2 F. Schwierz, J. Pezoldt and R. Granzner, *Nanoscale*, 2015, **7**, 8261–8283.
3 L. K. Li, Y. J. Yu, G. J. Ye, Q. Q. Ge, X. D. Ou, H. Wu, D. L. Feng, X. H. Chen and Y. B. Zhang, *Nat. Nanotechnol.*, 2014, **9**, 372–377.
4 K. S. Novoselov, A. Mishchenko, A. Carvalho and A. H.-C. Neto, *Science*, 2016, **353**, aac9439.
5 V. Nicolosi, M. Chhowalla, M. G. Kanatzidis, M. S. Strano and J. N. Coleman, *Science*, 2013, **340**, 1226419.
6 M. Naseri and S. R. Lin, *Chem. Phys. Lett.*, 2019, **722**, 58–63.
7 J. H. Yuan, Y. Q. Song, Q. Chen, K. H. Xue and X. S. Miao, *Appl. Surf. Sci.*, 2019, **469**, 456–462.
8 B. J. Feng, B. T. Fu, S. Kasamatsu, S. Ito, P. Cheng, C. C. Liu, Y. Feng, S. L. Wu, S. K. Mahatha, P. Sheverdyaeva, P. Moras, M. Arita, O. Sugino, T. C. Chiang, K. Shimada, K. Miyamoto, T. Okuda, K. H. Wu, L. Chen, Y. G. Yao and I. Matsuda, *Nat. Commun.*, 2017, **8**, 1–6.
9 Q. Xue, H. J. Zhang, M. S. Zhu, Z. X. Pei, H. F. Li, Z. F. Wang, Y. Huang, Y. Huang, Q. H. Deng, J. Zhou, S. Y. Du, Q. Huang and C. Y. Zhi, *Adv. Mater.*, 2017, **29**, 1604847.
10 L. F. Li, S. Z. Lu, J. B. Pan, Z. H. Qin, Y. Q. Wang, Y. L. Wang, G. Y. Cao, S. X. Du and H. J. Gao, *Adv. Mater.*, 2014, **26**, 4820–4824.
11 Q. H. Wang, K. Kalantar-Zadeh, A. Kis, J. N. Coleman and M. S. Strano, *Nat. Nanotechnol.*, 2012, **7**, 699–712.
12 Y. L. Li, A. Chernikov, X. Zhang, A. Rigosi, H. M. Hill, A. M. van der Zande, D. A. Chenet, E. M. Shih, J. Hone and T. F. Heinz, *Phys. Rev. B: Condens. Matter Mater. Phys.*, 2014, **90**, 205422.
13 J. K. Huang, J. Pu, C. L. Hsu, M. H. Chiu, Z. Y. Juang, Y. H. Chang, W. H. Chang, Y. Iwasa, T. Takenobu and L. J. Li, *ACS Nano*, 2014, **8**, 923–930.
14 Y. L. Jiao, L. J. Zhou, F. X. Ma, G. P. Gao, L. Z. Kou, J. Bell, S. Sanvito and A. J. Du, *ACS Appl. Mater. Interfaces*, 2016, **8**, 5385–5392.
15 Z. Y. Yin, H. Li, H. Li, L. Jiang, Y. M. Shi, Y. H. Sun, G. Lu, Q. Zhang, X. D. Chen and H. Zhang, *ACS Nano*, 2012, **6**, 74–80.
16 Y. Tian, A. Sun, Z. Z. Ge, Y. M. Zhang, S. L. Huang, S. H. Lv and H. P. Li, *Chem. Phys. Lett.*, 2021, **765**, 138286.
17 H. Jiang, *J. Phys. Chem. C*, 2012, **116**, 7664–7671.
18 R. L. Kautz, M. S. Dresselhaus and D. Adler, *Phys. Rev. B: Condens. Matter Mater. Phys.*, 1972, **6**, 2078–2082.
19 K. F. Mak, C. Lee, J. Hone, J. Shan and T. F. Heinz, *Phys. Rev. Lett.*, 2010, **105**, 136805.
20 R. Fivaz and E. Mooser, *Phys. Rev. A: At., Mol., Opt. Phys.*, 1967, **163**, 743–755.
21 S. Bertolazzi, J. Brivio and A. Kis, *ACS Nano*, 2011, **5**, 9703–9709.
22 E. W. Roberts, *Tribol. Int.*, 1990, **23**, 95–104.
23 C. Donnet, J. M. Martin, T. L. Mogne and M. Belin, *Tribol. Int.*, 1996, **29**, 123–128.
24 L. F. Wang, X. Zhou, T. B. Ma, D. M. Liu, L. Gao, X. Li, J. Zhang, Y. Z. Hu, H. Wang, Y. D. Dai and J. B. Luo, *Nanoscale*, 2017, **9**, 10846–10853.
25 B. Radisavljevic and A. Kis, *Nat. Mater.*, 2013, **12**, 815–820.
26 K. Chang, X. Hai, H. Pang, H. B. Zhang, L. Shi, G. G. Liu, H. M. Liu, G. X. Zhao, M. Li and J. H. Ye, *Adv. Mater.*, 2016, **28**, 10033–10041.
27 S. Wi, H. Kim, M. K. Chen, H. Nam, L. J. Guo, E. Meyhofer and X. G. Liang, *ACS Nano*, 2014, **8**, 5270–5281.
28 M. Dragoman, M. Aldrigo, D. Dragoman, I. M. Povey, S. Iordanescu, A. Dinescu, A. Di Donato and M. Modreanu, *Phys. E*, 2021, **126**, 114451.
29 H. L. Zeng, J. F. Dai, W. Yao, D. Xiao and X. D. Cui, *Nat. Nanotechnol.*, 2012, **7**, 490–493.
30 L. H. Yuwen, F. Xu, B. Xue, Z. M. Luo, Q. Zhang, B. Q. Bao, S. Su, L. X. Weng, W. Huang and L. H. Wang, *Nanoscale*, 2014, **6**, 5762–5769.
31 Y. F. Li, D. H. Wu, Z. Zhou, C. R. Cabrera and Z. F. Chen, *J. Phys. Chem. Lett.*, 2012, **3**, 2221–2227.
32 J. Y. Li, Y. Hou, X. F. Gao, D. S. Guan, Y. Y. Xie, J. H. Chen and C. Yuan, *Nano Energy*, 2015, **16**, 10–18.
33 J. Rehman, X. F. Fan, A. Laref, V. A. Dinh and W. T. Zheng, *J. Alloys Compd.*, 2021, **865**, 158782.
34 X. Q. Xie, S. J. Wang, K. Kretschmer and G. X. Wang, *J. Colloid Interface Sci.*, 2017, **499**, 17–32.
35 J. Y. Hao, J. F. Zheng, F. L. Ling, Y. K. Chen, H. R. Jing, T. W. Zhou, L. Fang and M. Zhou, *Sci. Rep.*, 2018, **8**, 2079.

36 X. D. Ren, Q. Zhao, W. D. McCulloch and Y. Y. Wu, *Nano Res.*, 2017, **10**, 1313–1321.
37 J. H. Li, B. L. Rui, W. X. Wei, P. Nie, L. M. Chang, Z. Y. Le, M. Q. Liu, H. R. Wang, L. M. Wang and X. G. Zhang, *J. Power Sources*, 2020, **449**, 227481.
38 S. Zheng, T. Yu, J. Y. Lin, H. Lou, H. Y. Xu and G. C. Yang, *J. Mater. Chem. A*, 2019, **7**, 25665–25671.
39 S. Zheng, C. X. Huang, T. Yu, M. L. Xu, S. T. Zhang, H. Y. Xu, Y. C. Liu, E. J. Kan, Y. C. Wang and G. C. Yang, *J. Phys. Chem. Lett.*, 2019, **10**, 2733–2738.
40 K. S. Chen, I. Balla, N. S. Luu and M. C. Hersam, *ACS Energy Lett.*, 2017, **2**, 2026–2034.
41 H. R. Jiang, Z. H. Lu, M. C. Wu, F. Ciucci and T. S. Zhao, *Nano Energy*, 2016, **23**, 97–104.
42 P. Poizot, S. Laruelle, S. Grugeon, L. Dupont and J. M. Tarascon, *Nature*, 2000, **407**, 496–499.
43 N. Yabuuchi, K. Kubota, M. Dahbi and S. Komaba, *Chem. Rev.*, 2014, **114**, 11636–11682.
44 Y. Y. Liu, B. V. Merinov and W. A. Goddard, *Proc. Natl. Acad. Sci. U. S. A.*, 2016, **113**, 3735–3739.
45 W. C. Zhang, J. F. Mao, S. A. Li, Z. X. Chen and Z. P. Guo, *J. Am. Chem. Soc.*, 2017, **139**, 3316–3319.
46 Z. L. Jian, W. Luo and X. L. Ji, *J. Am. Chem. Soc.*, 2015, **137**, 11566–11569.
47 G. Kresse and J. Hafner, *Phys. Rev. B: Condens. Matter Mater. Phys.*, 1993, **47**, 558–561.
48 G. Kresse and J. Hafner, *Phys. Rev. B: Condens. Matter Mater. Phys.*, 1994, **49**, 14251–14269.
49 G. Kresse and J. Furthmüller, *Comput. Mater. Sci.*, 1996, **6**, 15–50.
50 G. Kresse and J. Furthmüller, *Phys. Rev. B: Condens. Matter Mater. Phys.*, 1996, **54**, 11169–11186.
51 P. E. Blochl, *Phys. Rev. B: Condens. Matter Mater. Phys.*, 1994, **50**, 17953–17979.
52 J. P. Perdew, K. Burke and M. Ernzerhof, *Phys. Rev. Lett.*, 1996, **77**, 3865–3868.
53 J. Paier, R. Hirschl, M. Marsman and G. Kresse, *J. Chem. Phys.*, 2005, **122**, 234102.
54 H. J. Monkhorst and J. D. Pack, *Phys. Rev. B: Condens. Matter Mater. Phys.*, 1976, **13**, 5188–5192.
55 A. Togo and I. Tanaka, *Scr. Mater.*, 2015, **108**, 1–5.
56 G. J. Martyna, M. L. Klein and M. Tuckerman, *J. Chem. Phys.*, 1992, **97**, 2635–2643.
57 J. Heyd, G. E. Scuseria and M. Ernzerhof, *J. Chem. Phys.*, 2006, **124**, 8207–8215.
58 T. R. Galeev, B. D. Dunnington, J. R. Schmidt and A. I. Boldyrev, *Phys. Chem. Chem. Phys.*, 2013, **15**, 5022–5029.
59 J. Q. Yi, B. B. Gong, C. Xu, W. H. Zhang and L. J. Cheng, *Phys. Chem. Chem. Phys.*, 2021, **23**, 24294–24300.
60 Q. M. Liu, C. Y. Zhang, C. Xu, S. L. Hu and L. J. Cheng, *Phys. Chem. Chem. Phys.*, 2020, **22**, 3921–3926.
61 N. Fedik, D. V. Steglenko, A. Muñoz-Castro, R. M. Minyaev and V. I. Minkin, *J. Phys. Chem. C*, 2021, **125**, 17280–17290.
62 D. V. Steglenko, N. V. Tkachenko, A. I. Boldyrev, R. M. Minyaev and V. I. Minkin, *J. Comput. Chem.*, 2020, **41**, 1456–1463.
63 T. H. Dunning, *J. Chem. Phys.*, 1989, **90**, 1007–1023.
64 G. Henkelman, B. P. Uberuaga and H. Jónsson, *J. Chem. Phys.*, 2000, **113**, 9901–9904.
65 L. A. Burns, A. Vazquez-Mayagoitia, B. G. Sumpter and C. D. Sherrill, *J. Chem. Phys.*, 2011, **134**, 084107.
66 S. Grimme, *J. Comput. Chem.*, 2004, **25**, 1463–1473.
67 K. Momma and F. Izumi, *J. Appl. Crystallogr.*, 2011, **44**, 1272–1276.
68 F. Mouhat and F. X. Coudert, *Phys. Rev. B: Condens. Matter Mater. Phys.*, 2014, **90**, 224104.
69 C. Z. Zhang and Q. Sun, *J. Phys. Chem. Lett.*, 2016, **7**, 2664–2670.
70 E. Cadelano, P. L. Palla, S. Giordano and L. Colombo, *Phys. Rev. B: Condens. Matter Mater. Phys.*, 2010, **82**, 235414.
71 Q. Yue, J. Kang, Z. Shao, X. Zhang, S. Chang, G. Wang, S. Qin and J. Li, *Phys. Lett. A*, 2012, **376**, 1166–1170.
72 V. O. Ozcelik, O. U. Akturk, E. Durgun and S. Ciraci, *Phys. Rev. B: Condens. Matter Mater. Phys.*, 2015, **92**, 125420.
73 A. H. Woomer, T. W. Farnsworth, J. Hu, R. A. Wells, C. L. Donley and S. C. Warren, *ACS Nano*, 2015, **9**, 8869–8884.
74 Y. Guo, S. Zhou, Y. Z. Bai and J. J. Zhao, *ACS Appl. Mater. Interfaces*, 2017, **9**, 12013–12020.
75 T. Yu, Z. Y. Zhao, Y. H. Sun, A. Bergara, J. Y. Lin, S. T. Zhang, H. Y. Xu, L. J. Zhang, G. C. Yang and Y. C. Liu, *J. Am. Chem. Soc.*, 2019, **141**, 1599–1605.
76 R. Zacharia, H. Ulbricht and T. Hertel, *Phys. Rev. B: Condens. Matter Mater. Phys.*, 2004, **69**, 155406.
77 J. H. Jung, C. H. Park and J. Ihm, *Nano Lett.*, 2018, **18**, 2759–2765.
78 M. Long, A. Gao, P. Wang, H. Xia, C. Ott, C. Pan, Y. Fu, E. Liu, X. Chen, W. Lu, T. Nilges, J. Xu, X. Wang, W. Hu and F. Miao, *Sci. Adv.*, 2017, **3**, e1700589.
79 H. Zhang, Y. Li, J. Hou, K. Tu and Z. Chen, *J. Am. Chem. Soc.*, 2016, **138**, 5644–5651.
80 S. Thinius, M. M. Islam, P. Heitjans and T. Bredow, *J. Phys. Chem. C*, 2014, **118**, 2273–2280.
81 K. Dou, Y. Ma, T. Zhang, B. Huang and Y. Dai, *Phys. Chem. Chem. Phys.*, 2019, **21**, 26212–26218.
82 X. S. Lv, W. Wei, Q. L. Sun, L. Yu, B. B. Huang and Y. Dai, *ChemPhysChem*, 2017, **18**, 1627–1634.
83 Y. S. Meng and M. E. Arroyo-de Dompablo, *Energy Environ. Sci.*, 2009, **2**, 589–609.
84 E. Yang, H. Ji, J. Kim, H. Kim and Y. Jung, *Phys. Chem. Chem. Phys.*, 2015, **17**, 5000–5005.
85 C. Eames and M. S. Islam, *J. Am. Chem. Soc.*, 2014, **136**, 16270–16276.